

Strain-tunable Berry curvature in quasi-two-dimensional chromium telluride

Hang Chi,^{1,2,*} Yunbo Ou,^{1,†} Tim B. Eldred,³ Wenpei Gao,³ Sohee Kwon,⁴ Joseph Murray,⁵ Michael Dreyer,⁵ Robert E. Butera,⁶ Alexandre C. Foucher,⁷ Haile Ambaye,⁸ Jong Keum,^{8,9} Alice T. Greenberg,² Yuhang Liu,⁴ Mahesh R. Neupane,^{2,4} George J. de Coster,² Owen A. Vail,² Patrick J. Taylor,² Patrick A. Folkes,² Charles Rong,² Gen Yin,¹⁰ Roger K. Lake,⁴ Frances M. Ross,⁷ Valeria Lauter,⁸ Don Heiman,^{1,11} and Jagadeesh S. Moodera^{1,12,‡}

¹*Francis Bitter Magnet Laboratory, Plasma Science and Fusion Center, Massachusetts Institute of Technology, Cambridge, Massachusetts 02139, USA*

²*U.S. Army CCDC Army Research Laboratory, Adelphi, Maryland 20783, USA*

³*Department of Materials Science and Engineering, North Carolina State University, Raleigh, North Carolina 27695, USA*

⁴*Department of Electrical and Computer Engineering, University of California, Riverside, California 92521, USA*

⁵*Department of Physics, University of Maryland, College Park, Maryland 20742, USA*

⁶*Laboratory for Physical Sciences, College Park, Maryland 20740, USA*

⁷*Department of Materials Science and Engineering, Massachusetts Institute of Technology, Cambridge, Massachusetts 02139, USA*

⁸*Neutron Scattering Division, Neutron Sciences Directorate, Oak Ridge National Laboratory, Oak Ridge, Tennessee 37831, USA*

⁹*Center for Nanophase Materials Sciences, Physical Science Directorate, Oak Ridge National Laboratory, Oak Ridge, Tennessee 37831, USA*

¹⁰*Department of Physics, Georgetown University, Washington, District of Columbia 20057, USA*

¹¹*Department of Physics, Northeastern University, Boston, Massachusetts 02115, USA*

¹²*Department of Physics, Massachusetts Institute of Technology, Cambridge, Massachusetts 02139, USA*

(Dated: December 13, 2022)

Magnetic transition metal chalcogenides form an emerging platform for exploring spin-orbit driven Berry phase phenomena owing to the nontrivial interplay between topology and magnetism. Here we show that the anomalous Hall effect in pristine Cr_2Te_3 thin films manifests a unique temperature-dependent sign reversal at nonzero magnetization, resulting from the momentum-space Berry curvature as established by first-principles simulations. The sign change is strain tunable, enabled by the sharp and well-defined substrate/film interface in the quasi-two-dimensional Cr_2Te_3 epitaxial films, revealed by scanning transmission electron microscopy and depth-sensitive polarized neutron reflectometry. This Berry phase effect further introduces hump-shaped Hall peaks in pristine Cr_2Te_3 near the coercive field during the magnetization switching process, owing to the presence of strain-modulated magnetic domains. The versatile interface tunability of Berry curvature in Cr_2Te_3 thin films offers new opportunities for topological electronics.

In recent years, a variety of novel two-dimensional (2D) van der Waals magnets have been discovered, founding the active field of 2D magnetism [1]. Among these prospective compounds, binary chromium tellurides $\text{Cr}_{1-\delta}\text{Te}$ [2–8] are attractive owing to their rich magnetic properties, as well as inherent chemical and structural compatibility when forming heterostructures [9] with other topological systems, such as tetradymite-type topological insulators [10] or chalcogenide-based Dirac/Weyl semimetals [11]. Furthermore, the broken time-reversal symmetry and the strong spin-orbit coupling (SOC) offer unique opportunities for the interplay between spin configurations and reciprocal-space topology [12–14]. In this regard, ferromagnetic Cr_2Te_3 with strong perpendicular magnetic anisotropy (PMA) is an intriguing platform to host non-trivial topological physics, particularly for the high-quality thin films grown by molecular beam epitaxy (MBE) [15, 16].

An important consequence of the band topology in Cr_2Te_3 is the Berry curvature [17, 18] underlying the anomalous Hall effect (AHE) [19]. The intrinsic AHE is

topological in nature and a hallmark of itinerant ferromagnets, which has also been observed in more exotic systems even without a net magnetization, such as spin liquids [20], antiferromagnets [21] and Weyl semimetals [22]. When SOC coexists with long-range magnetic order, the Berry curvature can be significantly influenced near avoided band crossings, rendering the system an incredibly rich playground combining topology and magnetism [23, 24].

Here, we report the unique magnetotransport signatures of high-quality quasi-2D Cr_2Te_3 MBE grown thin films governed by non-trivial band topologies. Via synergistic structural, magnetic and transport measurements, together with first-principles simulations, we have uncovered novel Berry-curvature-induced magnetism featuring an extraordinary sign reversal of the AHE, as we modulate the temperature and the strain for the thin films containing 3 to 24 unit cells (u.c.) on $\text{Al}_2\text{O}_3(0001)$ or $\text{SrTiO}_3(111)$ substrates. Moreover, a hump-shaped Hall feature emerges, most likely due to the presence of multiple magnetic domains under different levels of inter-

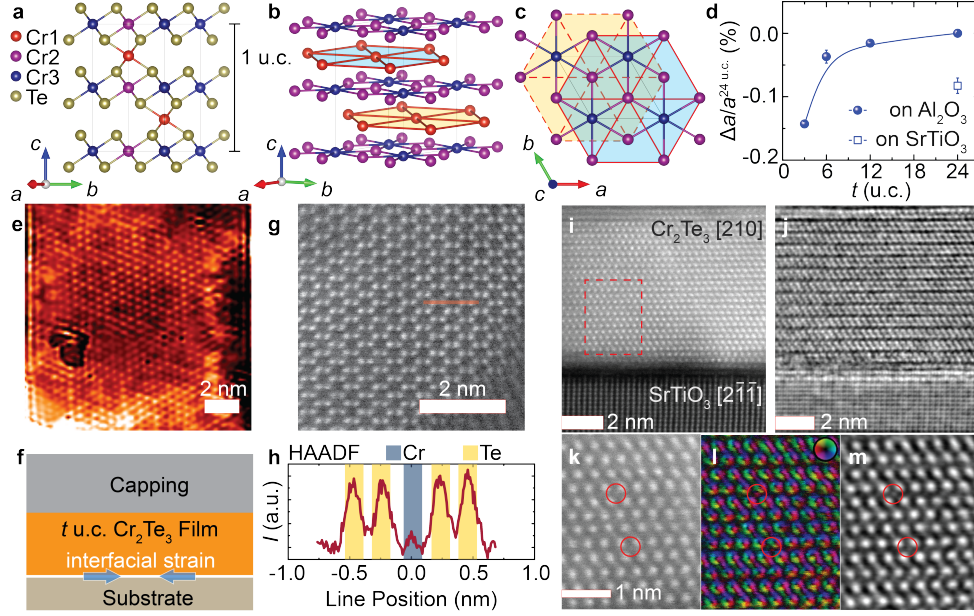


Figure 1 | Crystal structure of Cr₂Te₃ thin films. **a**, Atomistic structure of Cr₂Te₃ viewed along the crystallographic [210] direction. **b**, Among the three Cr species, Cr1 (red) form sparse honeycombs that are stacked between those of Cr2/Cr3 (purple/blue) with six-fold in-plane symmetry (**c**). **d**, Enhanced in-plane compressive strain at reduced thickness t , quantified by the relative change of the a lattice parameter via XRD for Cr₂Te₃ grown on Al₂O₃(0001) (solid) or SrTiO₃(111) (open). **f**, Schematic of the film stacks, where the interfacial strain plays a pivotal role in inducing extraordinary magnetic and transport phenomena. Atomically resolved STM morphology of a 13 × 13 nm² surface after removing Se capping (**e**) and planar HAADF STEM image (**g**) of Cr₂Te₃ confirm the honeycomb-like Te lattice, where the HAADF intensity line scan (**h**) reveals the Cr sites. **i-m**, Cross-sectional images of Cr₂Te₃ films grown on SrTiO₃(111). The HAADF (**i**) and iDPC (**j**) imaging along the [210] zone axis of Cr₂Te₃ illustrates the dominating Te-Cr2/Cr3-Te layers. The enlarged view (dashed box region in **i**) of HAADF (**k**), DPC (**l**), and iDPC (**m**) images identify the random distribution of the interlayer Cr1 (circles), which deviates from the ideal Cr₂Te₃ structure with full occupancy. The color wheel in the DPC image indicates the projected electric field direction.

facial strain. This work identifies pristine ferromagnetic Cr₂Te₃ thin films as a fascinating platform for further engineering topological effects given their nontrivial Berry curvature physics.

Atomic structure, interfaces and strain.

The crystalline structure of Cr₂Te₃ thin films is described first, followed by the development of strain at the substrate/film interface by the epitaxy. Bulk Cr₂Te₃ crystallizes in the structure with space group $P31c$ (D_{3d}^2 , No. 163), as shown in Figs. 1a-c, where each unit cell contains four vertically stacked hexagonal layers of Cr [25]. There are three symmetrically unique sites for Cr, labeled Cr1, Cr2 and Cr3, respectively: The Cr1 atoms are sparsely arranged in a weakly antiferromagnetic sublattice [26], while the Cr2/Cr3 atoms form ferromagnetic layers similar to those in CrTe₂ [27]. Since the Cr1 sites are often only partially filled (Figs. 1i-m), Cr₂Te₃ behaves essentially as a quasi-2D magnet [28–30]. This quasi-2D nature of Cr₂Te₃ allows for high-quality, layer-by-layer epitaxial growth of c -oriented films on a variety of substrates. The hexagonal c axis is the easy magnetic axis, leading to PMA for the films.

The six-fold in-plane (IP) symmetry is seen in the honeycombs visualized by atomic resolution scanning tunnel-

ing microscopy (STM, Fig. 1e) and scanning transmission electron microscopy (STEM, Fig. 1g) high-angle annular dark-field (HAADF) imaging, as well as in the reflection high-energy electron diffraction (RHEED, Supplementary Fig. 1) and X-ray diffraction (XRD, Supplementary Fig. 2) patterns. The sharp substrate/film interface is confirmed by the cross sectional HAADF (Fig. 1i) and the corresponding integrated differential phase contrast (iDPC, Fig. 1j) images. The intrinsic random distribution of Cr atoms on the Cr1 sites is resolved in the enlarged view of the atoms in Figs. 1k-m, shown overlaid with red circles, while the overall chemical composition of the thin film is uniform within the resolution of energy dispersive X-ray spectroscopy (EDS, see Supplementary Fig. 3).

Figure 1f illustrates the basic sample architecture, where the strain in the Cr₂Te₃ thin films is governed by the interface with the substrate. Upon reducing the thickness (t), films grown on Al₂O₃(0001) can develop an IP compressive strain up to -0.15% , as determined by XRD and summarized in Fig. 1d. A higher strain level can be sustained using SrTiO₃(111) substrates. Such control of strain is well suited for exploring interface-sensitive properties in Cr₂Te₃ thin films.

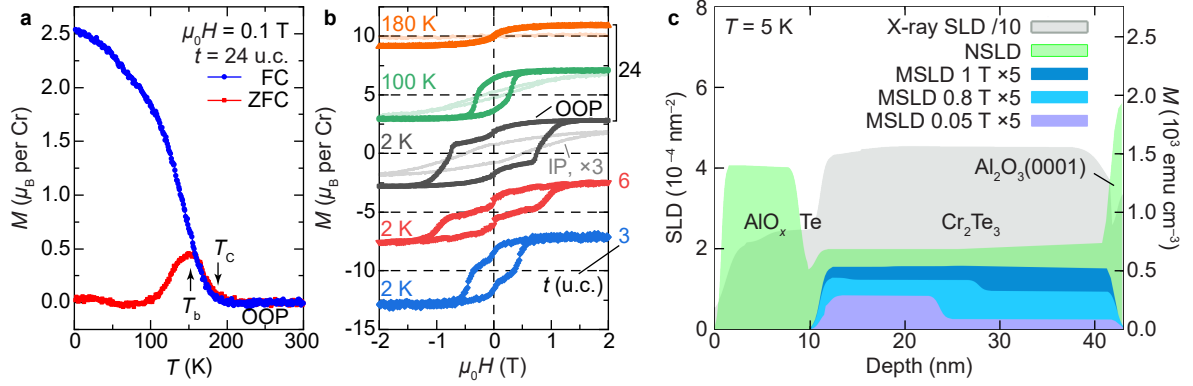


Figure 2 | Magnetic properties of Cr_2Te_3 thin films. **a**, Temperature dependence of the magnetization M of a typical 24 u.c. Cr_2Te_3 film under the zero-field-cool (ZFC) and field-cool (FC) conditions with an out-of-plane (OOP) external magnetic field $\mu_0 H = 0.1$ T. The Curie (T_C) and blocking (T_b) temperatures are labeled by the arrows. **b**, Field dependence of M under OOP and in-plane (IP) configurations for $t = 24$ u.c. at selected temperatures (top three, black, green and orange) and OOP $M(H)$ for $t = 6$ u.c. and 3 u.c. at 2 K (bottom two, red and blue). For clarity, the curves are vertically shifted and the IP data are magnified by a factor of 3. **c**, Depth profiles of PNR nuclear (NSLD), magnetic (MSLD, at IP fields of 1 T, 0.8 T and 0.05 T, respectively) and X-ray scattering length densities (SLD) of 24 u.c. Cr_2Te_3 on $\text{Al}_2\text{O}_3(0001)$ with Te/AlO_x capping.

Magnetism, domains and PNR.

The magnetic properties of Cr_2Te_3 thin films with selected thicknesses were assessed using vibrating sample magnetometry (VSM). Figure 2a shows the temperature dependence of the magnetization $M(T)$ for a $t = 24$ u.c. film on $\text{Al}_2\text{O}_3(0001)$ substrate with an out-of-plane (OOP) applied magnetic field $\mu_0 H = 0.1$ T. Under the field-cool (FC) condition, $M(T)$ rises below the Curie temperature $T_C \sim 180$ K, reaching $M \sim 2.50 \mu_B$ (Bohr magneton) per Cr at 2 K in the 0.1 T field. The zero-field-cool (ZFC) scan on the other hand deviates from the FC curve below the blocking temperature T_b , signaling the freezing out of domains in random direction in the absence of an aligning field H .

As illustrated in Fig. 2b, Cr_2Te_3 favors PMA with coercive field $\mu_0 H_c = 0.76$ T and saturation magnetization $M_s \sim 2.83 \mu_B$ per Cr at 2 K for $t = 24$ u.c., whereas the IP measurements have weaker ferromagnetic hysteresis loops. The low- T zero-field kink in the OOP $M(H)$ becomes more prominent at reduced t (for additional data on $t = 6$ u.c., see Supplementary Fig. 4), indicating the presence of interfacial strain-induced multiple magnetic domains with continuously varying spin canting [31–33].

Depth-sensitive polarized neutron reflectometry (PNR) measurements, responsive to the IP magnetization, were carried out at chosen T and H on samples with $t = 24$ and 6 u.c., in order to uncover the impact of interfacial strain. The PNR spin asymmetry ratio $SA = (R^+ - R^-)/(R^+ + R^-)$, measured as a function of the wave vector transfer $Q = 4\pi \sin(\theta)/\lambda$ with R^+ and R^- being the reflectivity for the neutron spin parallel (+) or antiparallel (−) to the external field, evidently confirms the magnetization (Supplementary Fig. 5). By simultaneously refining PNR and X-ray reflectivity

(XRR, Supplementary Fig. 5) data, the depth profiles of nuclear (NSLD) and magnetic (MSLD) scattering length densities (SLD) at $\mu_0 H = 1$ T, 0.8 T and 0.05 T for $t = 24$ u.c. were obtained and shown in Fig. 2c. The uniform MSLD profile at the IP saturation field $\mu_0 H = 1$ T attests to the high quality of the magnetic Cr_2Te_3 layer with well-defined interfaces of 0.5 nm. Remarkably, at a reduced IP field $\mu_0 H = 0.8$ T and 0.05 T, M develops a non-uniform depth-dependent magnetization profile with two components, revealing a lower (higher) value close to (away from) the substrate. Since PNR is sensitive to IP magnetization, these results collectively suggest that more pronounced strain at the interface leads to a higher OOP magnetic anisotropy and hence a lower measured IP MSLD. This scenario is further substantiated by the lower M observed for $t = 6$ u.c. with stronger strain measured at 5 K and 60 K under 1 T IP magnetic field (Supplementary Fig. 4d). The salient structural and magnetic features pave the way for an in-depth investigation of the magneto-transport responses in Cr_2Te_3 thin films.

Strain-tunable AHE and sign reversal.

The unusual Hall effects are the most outstanding properties of the Cr_2Te_3 thin films. The development of long-range magnetic ordering is manifested in the AHE-induced hysteresis in the Hall resistivity

$$\rho_{yx}(H) = R_H + R_S M, \quad (1)$$

in Fig. 3a (for more details on the transport parameters, see Supplementary Fig. 6). Here R_H characterizes the linear-in- H ordinary Hall effect (OHE) that dominates at high H and R_S is the AHE coefficient denoting contribution from the underlying magnetic order.

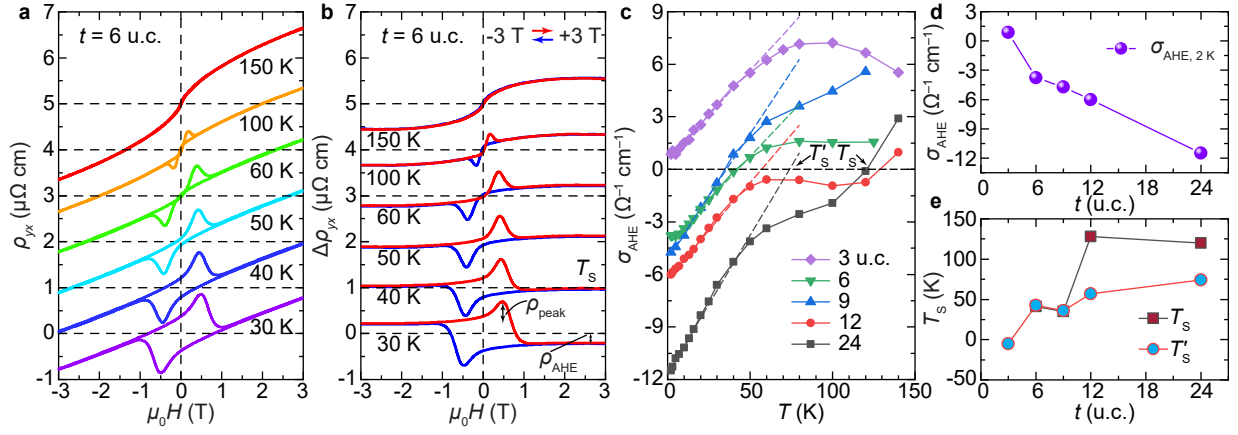


Figure 3 | The unconventional Hall effects in Cr_2Te_3 thin films. **a**, Magnetic field dependence of the Hall resistivity $\rho_{yx}(H)$ at selected temperatures of 6 u.c. Cr_2Te_3 on $\text{Al}_2\text{O}_3(0001)$. **b**, Hall traces $\Delta\rho_{yx}$ after removing the high-field ordinary Hall backgrounds. At $T_S \sim 40$ K, a sign change occurs in the anomalous Hall resistivity ρ_{AHE} , defined as the value of $\Delta\rho_{yx}$ when the system is fully magnetized under a positive H . Apart from the AHE hysteresis loop, additional hump-shaped features develop. **c**, Temperature dependence of the anomalous Hall conductivity σ_{AHE} for $t = 3 - 24$ u.c. (symbols, where solid lines are guide for the eye and dashed lines are linear fit to the low T data). **d-e**, Thickness dependence of σ_{AHE} at 2 K (**d**), AHE sign reversal temperature T_S (**e**) and T'_S , the T -intercept of the linear AHE component at low T .

By removing the linear OHE background in Fig. 3a, we now turn to the rich T and H dependences of the Hall traces $\Delta\rho_{yx}(H)$ and the unconventional AHE in the ferromagnetic regime in Fig. 3b. For $t = 6$ u.c., at $T \leq 30$ K, when fully magnetized under a positive H , the system produces a negative AHE signal ρ_{AHE} , i.e., $\Delta\rho_{yx}(H)$ loops around the origin in the opposite direction of that for the $M(H)$ hysteresis (see Supplementary Fig. 4b). The T dependence of the corresponding anomalous Hall conductivity $\sigma_{\text{AHE}} = \rho_{\text{AHE}}/(\rho_{\text{AHE}}^2 + \rho_{xx}^2)$, with ρ_{xx} being the longitudinal electrical resistivity, is summarized in Fig. 3c. Upon rising T , ρ_{AHE} surprisingly changes sign at a transition temperature $T_S \sim 40$ K for $t = 6$ u.c.. Note that the sign change signifies a compensation point at T_S where ρ_{AHE} or the anomalous Hall conductivity σ_{AHE} traverses through zero while M remains finite (see Supplementary Fig. 7b). This is a highly unusual behavior, although rather similar to the transport anomaly present in SrRuO_3 as a result of the nontrivial band topology [23]. Furthermore, this unique sign reversal behavior of the AHE is sensitively governed by the interfacial strain (Fig. 3d). As evident in Fig. 3e, T_S largely decreases upon increasing compressive strain at reduced t (Fig. 1d). At $t = 3$ u.c., the strain is found to be sufficient in driving $\sigma_{\text{AHE}} > 0$ in the ground state, leading to the absence of a temperature-induced sign flipping at finite T .

To elucidate the physical origin of the AHE sign reversal of Cr_2Te_3 , we examined the Berry curvature $\Omega^z(\mathbf{k}) = \sum_n f_n \Omega_n^z(\mathbf{k})$ (Fig. 4a, summed over the occupied bands with f_n the equilibrium Fermi-Dirac distribution function) based on the electronic band structure (Fig. 4b) obtained using density functional theory (DFT). As exemplified by the left inset of Fig. 4a, a significant spike

feature develops in $\Omega^z(\mathbf{k})$, originating from the nearly degenerate SOC anti-crossing bands along the A-L k -path. The intrinsic AHE conductivity is evaluated by integrating over the Brillouin zone (BZ)

$$\sigma_{\text{AHE}} = -\frac{e^2}{\hbar} \int_{\text{BZ}} \frac{d^3k}{(2\pi)^3} \Omega^z(\mathbf{k}), \quad (2)$$

where e is the electron charge and \hbar is the reduced Planck's constant. As shown in Fig. 4c, the calculated $\sigma_{\text{AHE}} = -12.7 \Omega^{-1} \text{ cm}^{-1}$ at the Fermi level ε_F for Cr_2Te_3 under equilibrium state (the black curve in Fig. 4c, see also Supplementary Fig. 8 for the convergence test under different k -mesh), which is in excellent agreement with the experimental value of $-11.5 \Omega^{-1} \text{ cm}^{-1}$ for $t = 24$ u.c.. It attests to the dominance of the intrinsic Berry phase mechanism, rather than the extrinsic side jump or skew scattering [19], as the primary origin of the observed AHE in Cr_2Te_3 . The calculation also reveals a sensitive energy dependence of σ_{AHE} – not only the magnitude but also the sign changes near ε_F . At finite T , due to the thermal broadening in f_n , the slight asymmetry of σ_{AHE} above and below ε_F , naturally explains the experimentally observed AHE sign anomaly. Modeling of strained cases in Fig. 4c further reveals that σ_{AHE} at ε_F changes sign under -1% compressive strain, substantiating that Berry physics underlies the observed strain-driven AHE sign reversal in Fig. 3d. This unique capability of achieving zero σ_{AHE} or ρ_{AHE} while maintaining nonzero M in Cr_2Te_3 thin films, deviating from the classic Eq. (1), offers direct insight into the intrinsic AHE solely owing to the Berry curvature [19, 34].

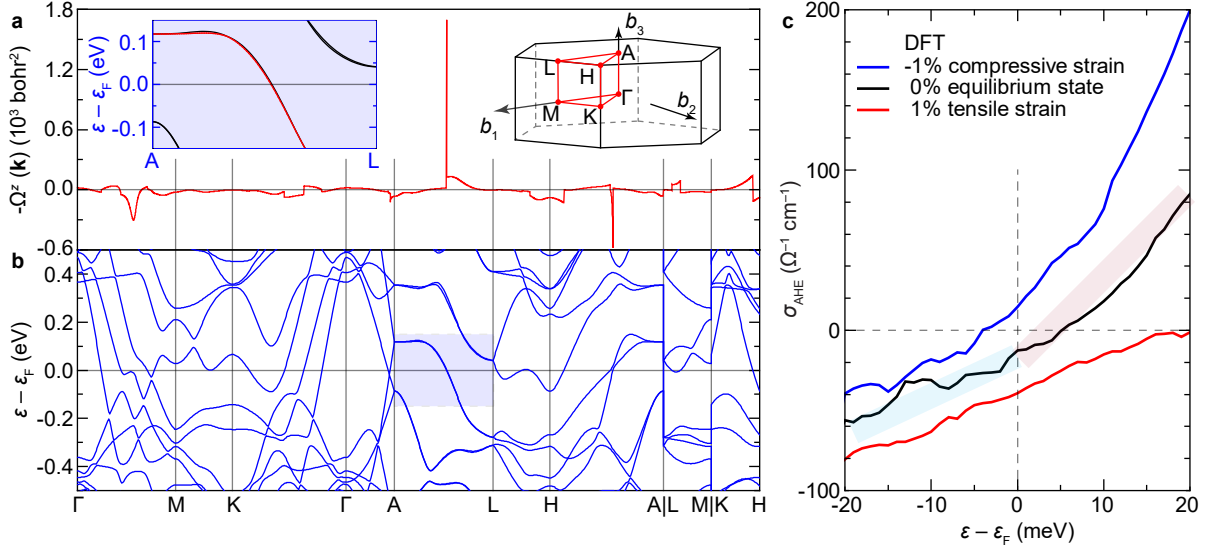


Figure 4 | Berry curvature and anomalous Hall conductivity in Cr_2Te_3 . **a-b**, Calculated Berry curvature $\Omega^z(\mathbf{k})$ (a) along the high symmetry k -paths in the Brillouin zone (right inset in a) and the corresponding electronic band structure (b). Left inset in a, nearly degenerate SOC anti-crossing bands contributing to the sharp peak in $\Omega^z(\mathbf{k})$ along A-L. **c**, Anomalous Hall conductivity σ_{AHE} near the Fermi level ε_F , in equilibrium state (black), under compressive (blue) or tensile (red) strain conditions, respectively. The shades in c are guide for the eye showing the slight asymmetry of the energy dependence of σ_{AHE} above and below ε_F which at finite T may lead to a sign reversal in σ_{AHE} owing to thermal broadening.

Hump-shaped Hall peaks at the coercive field.

Figure 3b also shows additional hump-shaped peaks on top of the otherwise square AHE hysteresis loop. The peaks are centered at the characteristic fields H_{peak} that tracks well with the coercive fields H_c determined from the magnetic measurements (Supplementary Fig. 7). These hump-shaped Hall peaks in our pristine Cr_2Te_3 are related to the presence of strain-modulated magnetic multidomain structures with opposite signs of AHE (Fig. 5a), rather than the skyrmion-induced topological Hall effect as postulated in various related phases and heterostructures [35–41]. To better understand the mechanism(s) underlying the Hall peaks observed in $\Delta\rho_{yx}(H)$, minor loop experiments were carried out for $t = 6$ u.c. at $T = 30$ K and are shown in Fig. 5b. For each scan, the loop starts from a well-defined initial state that is fully magnetized under a positive H , which is then swept towards a negative H_{min} around $-H_{\text{peak}}$ and scanned back to the initial positive H . The minor loops are hysteretic, where the emergence of the Hall peak with positive H depends on whether H_{min} surpasses $-H_{\text{peak}}$. The two-component origin of the Hall anomaly peaks can be quite well explained by a distribution of domains having T -dependent H_c using [42]

$$\Delta\rho_{yx}(H) = \int_0^\infty \tilde{\rho}_{\text{AHE}}(T') \{2H_{\text{Heav}}[H - \tilde{H}_c(T')] - 1\} G(T') dT' \quad (3)$$

Here $\tilde{\rho}_{\text{AHE}}(T')$ and $\tilde{H}_c(T')$ are functionals based on experimental ρ_{AHE} and H_c (Fig. 3c and Supplementary Fig. 7), $H_{\text{Heav}}(x)$ is the Heaviside function approximat-

ing the switching of M , and the Gaussian distribution

$$G(T') = \frac{1}{\sqrt{2\pi T_\sigma^2}} \exp \left[-\frac{(T' - T)^2}{2T_\sigma^2} \right], \quad (4)$$

characterizes the strain-driven distribution of domains with varying T_S by assuming an effective temperature spreading factor T_σ . As compared in Fig. 5c, the numerical simulation indeed reproduces qualitatively well the behavior of the minor loops. The observed AHE sign change and the emergence of hump-shaped Hall features are also present in films grown on $\text{SrTiO}_3(111)$ (Supplementary Fig. 9). The quality of the substrate/film interface plays a pivotal role in materializing this exquisite tunability of the Berry curvature in Cr_2Te_3 films.

In summary, we have discovered several unusual Berry curvature driven effects in the anomalous Hall transport of Cr_2Te_3 thin films. We report on the growth, detailed magnetic and transport properties of pristine Cr_2Te_3 MBE thin films deposited on $\text{Al}_2\text{O}_3(0001)$ and $\text{SrTiO}_3(111)$ substrates. A striking sign reversal in the anomalous Hall resistivity, accompanied by a finite magnetization, has been observed and theoretically modeled, revealing the relevance of the nontrivial Berry curvature physics. This unique sign reversal, coupled with the intrinsic strain-modulated magnetic domains in the material, induces a hump-shaped Hall feature in Cr_2Te_3 thin films. The Berry curvature effect is observed in this case due to the high quality of the substrate/film interface, which is further tunable via different level of

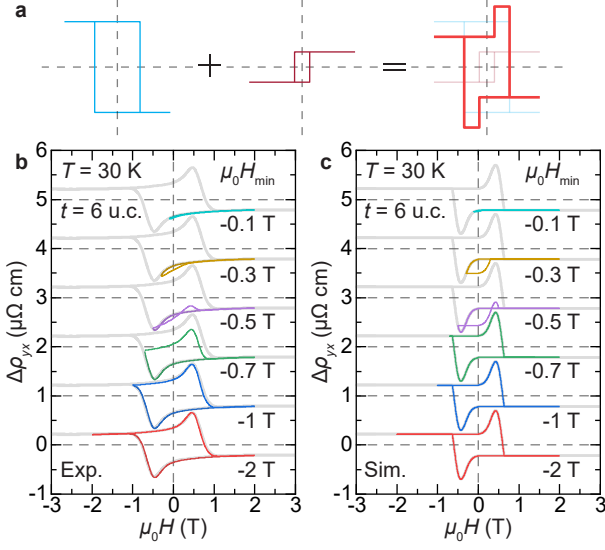


Figure 5 | Characteristics of hump-shaped Hall peaks. **a**, Simplified superposition of two AHE components with opposite sign and different coercive fields. **b-c**, Minor loop experiments on a 6 u.c. Cr_2Te_3 on $\text{Al}_2\text{O}_3(0001)$ at $T = 30\text{ K}$, first fully magnetized at $\mu_0 H = +3\text{ T}$ (complete loop shown in grey as guide for the eye) and then swept back and forth between $+2\text{ T}$ and selected $\mu_0 H_{\min}$. The experimental minor loops in **b** are qualitatively reproduced in **c** using simulations that underscore the significance of strain-driven multidomain features and the sign reversal in ρ_{AHE} .

strain given by varying film thickness and/or choice of substrates. Our comprehensive experimental and theoretical investigations establish Cr_2Te_3 to host tunable topological effects related to the intrinsic Berry curvature, thereby providing new perspectives in the field of topological electronics.

METHODS

Sample growth. The growth of Cr_2Te_3 thin films, with nominal t ranging from 3 – 24 u.c. were carried out in a MBE system under an ultrahigh-vacuum (UHV) environment of $10^{-10} - 10^{-9}$ Torr. Insulating $\text{Al}_2\text{O}_3(0001)$ was primarily used as substrate, whose surface quality was insured by *ex situ* chemical and thermal cleaning and *in situ* outgassing at 800°C for 30 min. When using $\text{SrTiO}_3(111)$, the insulating substrates were first annealed at 930°C for 3 hours in a tube furnace under flowing oxygen environment to achieve passivated surface with atomic flatness and then *in situ* outgassed at 580°C for 30 min. After surface preparation, the substrate temperature was lowered to 230°C for film growth, allowing enough surface mobility for the epitaxial crystallization of the desired phase of Cr_2Te_3 . High-purity (5N) Cr was evaporated from an electron-beam source, while Te was thermally co-evaporated from a Knudsen effusion cell ad-

justed to maintain a typical Cr:Te flux ratio of 1:10 and a growth rate of approximately 0.005 nm s^{-1} . The epitaxial growth process was monitored by *in situ* RHEED (see Supplementary Fig. 1) operated at 15 kV. The as-grown films were *in situ* annealed at the growth temperature for 30 min, and naturally cooled to room temperature. For *ex situ* characterizations, films were protected by *in situ* capping with Te (2 nm) and AlO_x (10 nm) or Se (20 nm) for later removal for STM measurements. The schematic of film stack is illustrated in Fig. 1f.

Structural characterizations. The XRD patterns were obtained using a parallel beam of $\text{Cu K}\alpha_1$ radiation with wavelength $\lambda = 0.15406\text{ nm}$ in a Rigaku SmartLab system. The 2θ (for OOP measurement) and/or $2\theta_\chi$ (for IP configuration) scan angles were between 10° and 120° with a typical step size of 0.05° . XRR measurements were performed at the Center for Nanophase Materials Sciences (CNMS), Oak Ridge National Laboratory, on a PANalytical X’Pert Pro MRD equipped with hybrid monochromator and Xe proportional counter. For the XRR measurements, the X-ray beam was generated at 45 kV/40 mA, and the X-ray beam wavelength after the hybrid mirror was $\lambda = 0.15406\text{ nm}$ ($\text{Cu K}\alpha_1$ radiation). To facilitate electron microscopy, planner samples were deposited on Si_3N_4 TEM grids with thin Sb_2Te_3 buffer while cross-sectional samples were prepared using focused ion beam (FIB) lift-out method on a Thermo Scientific FEI Quanta 3D dual beam system. STEM imaging was carried out on a Thermo Scientific FEI Titan aberration-corrected system operated at 200 kV. A semi-convergence angle of 17.9 mrad was used. DPC and iDPC images were recorded using a segmented detector. For the 3 u.c. sample, STEM images were acquired with a Themis Z G3 instrument provided by Thermo Fischer Scientific at 200 kV with a beam current of 40 pA and a convergence angle of 25 mrad .

Scanning tunneling microscopy. STM experiments were performed at the Laboratory for Physical Sciences using a home-built low-temperature scanning tunneling microscope [43] controlled by a Topometrix digital feedback electronic control unit. Samples were loaded into an UHV environment with a base pressure of 5×10^{-10} Torr and heated in front of a residual gas analyzer to verify the removal of the Se capping layer before being transferred to the microscope at 77 K . Scans were performed with an electrochemically-etched tungsten tip and differential spectroscopy data were extracted via a Stanford Research Systems SR830 lock-in amplifier.

Polarized neutron reflectometry. PNR is a highly penetrating depth-sensitive technique to probe the chemical and magnetic depth profiles with a resolution of 0.5 nm . The depth profiles of the NSLD and MSLD correspond to the depth profile of the chemical and IP magnetization vector distributions on the atomic scale, respectively [44–46]. Based on these neutron scattering merits, PNR serves as the powerful technique to simulta-

neously and nondestructively characterize chemical and magnetic nature of buried interfaces [47]. PNR experiments were performed on the Magnetism Reflectometer at the Spallation Neutron Source at Oak Ridge National Laboratory [48–50], using neutrons with wavelengths λ in a band of 0.2 – 0.8 nm and a high polarization of 98.5–99%. Measurements were conducted in a closed cycle refrigerator (Advanced Research System) equipped with a 1.15 T Bruker electromagnet. Using the time-of-flight method, a collimated polychromatic beam of polarized neutrons with the wavelength band $\delta\lambda$ impinges on the film at a grazing angle θ , interacting with atomic nuclei and the spins of unpaired electrons. The reflected intensity R^+ and R^- are measured as a function of momentum transfer, $Q = 4\pi \sin(\theta)/\lambda$, with the neutron spin parallel (+) or antiparallel (–), respectively, to the applied field. To separate the nuclear from the magnetic scattering, the spin asymmetry ratio $SA = (R^+ - R^-)/(R^+ + R^-)$ is calculated, for which $SA = 0$ designating no magnetic moment in the system. Being electrically neutral, spin-polarized neutrons penetrate the entire multilayer structures and probe magnetic and structural composition of the film and buried interfaces down to the substrate.

Transport and magnetic measurements. Electrical transport measurements as a function of temperature, field and angle were performed in the temperature range of 2 – 300 K in a Quantum Design Physical Property Measurement System (PPMS) equipped with a 9 T superconducting magnet. A typical ac current (I_x) of 5 μA was injected into the Hall bar ($\sim 0.3 \times 1.0 \text{ mm}^2$ for hand-scratched or $10 \times 30 \text{ }\mu\text{m}^2$ for e-beam patterned) residing in the crystallographic a - b plane, while longitudinal (V_x) and transverse (V_y) voltages were simultaneously monitored using a lock-in technique. For aligning the magnetic field \mathbf{H} , a horizontal rotator was used with an angular resolution of $\sim 0.1^\circ$. VSM was used to characterize the magnetization, where linear diamagnetic backgrounds from sample holders/substrates were subtracted to obtain $M(H)$ and $M(T)$.

Theoretical simulations. First-principles calculations were performed using the Quantum Espresso packages [51]. The generalized gradient approximation with the Perdew-Burke-Ernzerhof parameterization (GGA-PBE) was used as the exchange-correlation functional [52]. An energy cutoff of 40 Ry and a $6 \times 6 \times 4$ Γ -centered k -mesh were applied for the relaxation calculation. The crystal structure of Cr_2Te_3 was fully optimized until the force on each atom is smaller than 0.05 eV nm^{-1} . The optimized lattice constants of bulk Cr_2Te_3 are $a = b = 0.6799 \text{ nm}$ and $c = 1.2022 \text{ nm}$. For the self-consistent field calculation, SOC was included and a higher $12 \times 12 \times 8$ k -mesh was used. The magnetization was set along the $-z$ axis. The resulting absolute magnetic moments of the Cr atoms are 3.08, 2.99 and 3.06 μ_B for Cr1, Cr2 and Cr3, respectively. For the Berry curvature and anomalous Hall conductivity calculations, the Wannier90 packages

were used [53]. Maximally localized Wannier functions (MLWF) including both Cr d -orbitals and Te p -orbitals were employed to reproduce the DFT-calculated band structure with SOC.

Data availability. The data that support the findings of this study are available from the corresponding author upon reasonable request.

ACKNOWLEDGMENTS

The work at MIT was supported by Army Research Office (W911NF-20-2-0061 and DURIP W911NF-20-1-0074), National Science Foundation (NSF-DMR 1700137) and Office of Naval Research (N00014-20-1-2306). H.C. was sponsored by the Army Research Laboratory (ARL) under Cooperative Agreement Number W911NF-19-2-0015. Y.O. and J.S.M. thank the Center for Integrated Quantum Materials (NSF-DMR 1231319) for financial support. D.H. thanks support from NSF grant DMR-1905662 and the Air Force Office of Scientific Research award FA9550-20-1-0247. T.B.E. is partially supported by NSF under Grant No. DGE 1633587. The electron microscopy was performed at the Analytical Instrumentation Facility (AIF) at North Carolina State University, which is supported by the State of North Carolina and NSF (Award No. ECCS-2025064). The AIF is a member of the North Carolina Research Triangle Nanotechnology Network (RTNN), a site in the National Nanotechnology Coordinated Infrastructure (NNCI). This work was carried out with the use of facilities and instrumentation supported by NSF through the Massachusetts Institute of Technology Materials Research Science and Engineering Center DMR - 1419807. This work was carried out in part through the use of MIT.nano’s facilities. This project was funded by the MIT-IBM Watson AI Lab. This research used resources at the Spallation Neutron Source, a Department of Energy Office of Science User Facility operated by the Oak Ridge National Laboratory. XRR measurements were conducted at the Center for Nanophase Materials Sciences (CNMS), which is a DOE Office of Science User Facility. STM measurements utilized the facilities and resources of the Laboratory for Physical Sciences. The DFT work was supported in part by the ARL Research Associateship Program (RAP) Cooperative Agreement Number W911NF-16-2-0008 and used the Extreme Science and Engineering Discovery Environment (XSEDE) supported by NSF Grant No. ACI-1548562 and allocation ID TG-DMR130081.

AUTHOR CONTRIBUTIONS

H.C., Y.O. and J.S.M. conceived and designed the research. H.C. grew the films with assistance from Y.O.,

J.S.M., C.R. and P.J.T., carried out magnetization measurements with D.H., collected and analyzed transport data on macroscopic initial Hall bars as well as microdevices fabricated by O.A.V., T.B.E., W.G., A.C.F. and F.M.R. examined the microstructure using STEM. J.M., M.D. and R.E.B. characterized the surface using STM. J.K. performed XRR measurements, V.L. and H.A. conducted PNR experiments, V.L. analyzed XRR and PNR data. S.K., Y.L., M.R.N., G.Y. and R.K.L. conducted first-principles calculations while A.T.G., G.J.d.C. and P.A.F. simulated micromagnetic responses. H.C., D.H. and J.S.M. wrote the manuscript, with contributions from all authors.

* chihang@mit.edu

† ybou@mit.edu

‡ moodera@mit.edu

- [1] K. S. Burch, D. Mandrus, and J.-G. Park, Magnetism in two-dimensional van der Waals materials, *Nature* **563**, 47 (2018).
- [2] H. Ipser, K. L. Komarek, and K. O. Klepp, Transition metal-chalcogen systems viii: The Cr-Te phase diagram, *Journal of the Less Common Metals* **92**, 265 (1983).
- [3] M. A. McGuire, V. O. Garlea, S. Kc, V. R. Cooper, J. Yan, H. Cao, and B. C. Sales, Antiferromagnetism in the van der Waals layered spin-lozenge semiconductor CrTe₃, *Physical Review B* **95**, 144421 (2017).
- [4] X. Zhang, Q. Lu, W. Liu, W. Niu, J. Sun, J. Cook, M. Vaninger, P. F. Miceli, D. J. Singh, S.-W. Lian, T.-R. Chang, X. He, J. Du, L. He, R. Zhang, G. Bian, and Y. Xu, Room-temperature intrinsic ferromagnetism in epitaxial CrTe₂ ultrathin films, *Nature Communications* **12**, 2492 (2021).
- [5] Y. Liu and C. Petrovic, Anomalous Hall effect in the trigonal Cr₅Te₈ single crystal, *Physical Review B* **98**, 195122 (2018).
- [6] Y. Wen, Z. Liu, Y. Zhang, C. Xia, B. Zhai, X. Zhang, G. Zhai, C. Shen, P. He, R. Cheng, L. Yin, Y. Yao, M. Getaye Sendeku, Z. Wang, X. Ye, C. Liu, C. Jiang, C. Shan, Y. Long, and J. He, Tunable Room-Temperature Ferromagnetism in Two-Dimensional Cr₂Te₃, *Nano Letters* **20**, 3130 (2020).
- [7] G. Cao, Q. Zhang, M. Frontzek, W. Xie, D. Gong, G. E. Sterbinsky, and R. Jin, Structure, chromium vacancies, and magnetism in a Cr_{12-x}Te₁₆ compound, *Physical Review Materials* **3**, 125001 (2019).
- [8] R. Chua, J. Zhou, X. Yu, W. Yu, J. Gou, R. Zhu, L. Zhang, M. Liu, M. B. H. Breese, W. Chen, K. P. Loh, Y. P. Feng, M. Yang, Y. L. Huang, and A. T. S. Wee, Room Temperature Ferromagnetism of Monolayer Chromium Telluride with Perpendicular Magnetic Anisotropy, *Advanced Materials* **33**, 2103360 (2021).
- [9] C. Gong and X. Zhang, Two-dimensional magnetic crystals and emergent heterostructure devices, *Science* **363**, eaav4450 (2019).
- [10] M. Z. Hasan and C. L. Kane, Colloquium: Topological insulators, *Reviews of Modern Physics* **82**, 3045 (2010).
- [11] N. P. Armitage, E. J. Mele, and A. Vishwanath, Weyl and Dirac semimetals in three-dimensional solids, *Reviews of Modern Physics* **90**, 15001 (2018).
- [12] J. Jiang, D. Xiao, F. Wang, J.-H. Shin, D. Andreoli, J. Zhang, R. Xiao, Y.-F. Zhao, M. Kayyalha, L. Zhang, K. Wang, J. Zang, C. Liu, N. Samarth, M. H. W. Chan, and C.-Z. Chang, Concurrence of quantum anomalous Hall and topological Hall effects in magnetic topological insulator sandwich heterostructures, *Nature Materials* **19**, 732 (2020).
- [13] B. A. Bernevig, C. Felser, and H. Beidenkopf, Progress and prospects in magnetic topological materials, *Nature* **603**, 41 (2022).
- [14] H. Chi and J. S. Moodera, Progress and prospects in the quantum anomalous hall effect, *APL Materials* **10**, 090903 (2022).
- [15] I. Žutić, J. Fabian, and S. Das Sarma, Spintronics: Fundamentals and applications, *Reviews of Modern Physics* **76**, 323 (2004).
- [16] Y. Tokura, K. Yasuda, and A. Tsukazaki, Magnetic topological insulators, *Nature Reviews Physics* **1**, 126 (2019).
- [17] R. Karplus and J. M. Luttinger, Hall Effect in Ferromagnetics, *Physical Review* **95**, 1154 (1954).
- [18] M. V. Berry, Quantal phase factors accompanying adiabatic changes, *Proceedings of the Royal Society of London. A. Mathematical and Physical Sciences* **392**, 45 (1984).
- [19] N. Nagaosa, J. Sinova, S. Onoda, A. H. MacDonald, and N. P. Ong, Anomalous Hall effect, *Reviews of Modern Physics* **82**, 1539 (2010).
- [20] Y. Machida, S. Nakatsuji, S. Onoda, T. Tayama, and T. Sakakibara, Time-reversal symmetry breaking and spontaneous Hall effect without magnetic dipole order, *Nature* **463**, 210 (2010).
- [21] Šmejkal, Libor and MacDonald, Allan H. and Sinova, Jairo and Nakatsuji, Satoru and Jungwirth, Tomas, Anomalous Hall antiferromagnets, *Nature Reviews Materials* **7**, 482 (2022).
- [22] T. Liang, J. Lin, Q. Gibson, S. Kushwaha, M. Liu, W. Wang, H. Xiong, J. A. Sobota, M. Hashimoto, P. S. Kirchmann, Z.-X. Shen, R. J. Cava, and N. P. Ong, Anomalous Hall effect in ZrTe₅, *Nature Physics* **14**, 451 (2018).
- [23] Z. Fang, N. Nagaosa, K. S. Takahashi, A. Asamitsu, R. Mathieu, T. Ogasawara, H. Yamada, M. Kawasaki, Y. Tokura, and K. Terakura, The Anomalous Hall Effect and Magnetic Monopoles in Momentum Space, *Science* **302**, 92 (2003).
- [24] K. Kim, J. Seo, E. Lee, K. T. Ko, B. S. Kim, B. G. Jang, J. M. Ok, J. Lee, Y. J. Jo, W. Kang, J. H. Shim, C. Kim, H. W. Yeom, B. Il Min, B.-J. Yang, and J. S. Kim, Large anomalous Hall current induced by topological nodal lines in a ferromagnetic van der Waals semimetal, *Nature Materials* **17**, 794 (2018).
- [25] M. Yuzuri, T. Kanomata, and T. Kaneko, The pressure effect on the Curie temperature and exchange striction of Cr₂S₃ and Cr₂Te₃, *Journal of Magnetism and Magnetic Materials* **70**, 223 (1987).
- [26] T. Hamasaki, T. Hashimoto, Y. Yamaguchi, and H. Watanabe, Neutron diffraction study of Cr₂Te₃ single crystal, *Solid State Communications* **16**, 895 (1975).
- [27] D. C. Freitas, R. Weht, A. Sulpice, G. Remenyi, P. Strobel, F. Gay, J. Marcus, and M. Núñez-Regueiro, Ferromagnetism in layered metastable 1T-CrTe₂, *Journal of Physics: Condensed Matter* **27**, 176002 (2015).

- [28] A. F. Andresen, The Magnetic Structure of Cr_2Te_3 , Cr_3Te_4 , and Cr_5Te_6 , *Acta Chemica Scandinavica* **24**, 3495 (1970).
- [29] M. Bester, I. Stefaniuk, and M. Kuzma, Quasi-Two-Dimensional Ferromagnetism in Cr_2Te_3 and Cr_5Te_8 Crystals, *Acta Physica Polonica A* **127**, 433 (2015).
- [30] A. Roy, S. Guchhait, R. Dey, T. Pramanik, C.-C. Hsieh, A. Rai, and S. K. Banerjee, Perpendicular Magnetic Anisotropy and Spin Glass-like Behavior in Molecular Beam Epitaxy Grown Chromium Telluride Thin Films, *ACS Nano* **9**, 3772 (2015).
- [31] H. Li, L. Wang, J. Chen, T. Yu, L. Zhou, Y. Qiu, H. He, F. Ye, I. K. Sou, and G. Wang, Molecular Beam Epitaxy Grown Cr_2Te_3 Thin Films with Tunable Curie Temperatures for Spintronic Devices, *ACS Applied Nano Materials* **2**, 6809 (2019).
- [32] A. L. Coughlin, D. Xie, Y. Yao, X. Zhan, Q. Chen, H. Hewa-Walpitage, X. Zhang, H. Guo, H. Zhou, J. Lou, J. Wang, Y. S. Li, H. A. Fertig, and S. Zhang, Near Degeneracy of Magnetic Phases in Two-Dimensional Chromium Telluride with Enhanced Perpendicular Magnetic Anisotropy, *ACS Nano* **14**, 15256 (2020).
- [33] I. H. Lee, B. K. Choi, H. J. Kim, M. J. Kim, H. Y. Jeong, J. H. Lee, S.-Y. Park, Y. Jo, C. Lee, J. W. Choi, S. W. Cho, S. Lee, Y. Kim, B. H. Kim, K. J. Lee, J. E. Heo, S. H. Chang, F. Li, B. L. Chittari, J. Jung, and Y. J. Chang, Modulating Curie Temperature and Magnetic Anisotropy in Nanoscale-Layered Cr_2Te_3 Films: Implications for Room-Temperature Spintronics, *ACS Applied Nano Materials* **4**, 4810 (2021).
- [34] Y. Fujisawa, M. Pardo-Almanza, C. H. Hsu, A. Mohamed, K. Yamagami, A. Krishnadas, F. C. Chuang, K. H. Khoo, J. Zang, A. Soumyanarayanan, and Y. Okada, Widely Tunable Berry curvature in the Magnetic Semimetal $\text{Cr}_{1+\delta}\text{Te}_2$, [arXiv:2204.02518](https://arxiv.org/abs/2204.02518) (2022).
- [35] D. Zhao, L. Zhang, I. A. Malik, M. Liao, W. Cui, X. Cai, C. Zheng, L. Li, X. Hu, D. Zhang, J. Zhang, X. Chen, W. Jiang, and Q. Xue, Observation of unconventional anomalous Hall effect in epitaxial CrTe thin films, *Nano Research* **11**, 3116 (2018).
- [36] J. Chen, L. Wang, M. Zhang, L. Zhou, R. Zhang, L. Jin, X. Wang, H. Qin, Y. Qiu, J. Mei, F. Ye, B. Xi, H. He, B. Li, and G. Wang, Evidence for Magnetic Skyrmions at the Interface of Ferromagnet/Topological-Insulator Heterostructures, *Nano Letters* **19**, 6144 (2019).
- [37] L. Zhou, J. Chen, X. Chen, B. Xi, Y. Qiu, J. Zhang, L. Wang, R. Zhang, B. Ye, P. Chen, X. Zhang, G. Guo, D. Yu, J.-W. Mei, F. Ye, G. Wang, and H. He, Topological Hall Effect in Traditional Ferromagnet Embedded with Black-Phosphorus-Like Bismuth Nanosheets, *ACS Applied Materials & Interfaces* **12**, 25135 (2020).
- [38] X. Zhang, S. C. Ambhire, Q. Lu, W. Niu, J. Cook, J. S. Jiang, D. Hong, L. Alahmed, L. He, R. Zhang, Y. Xu, S. S. L. Zhang, P. Li, and G. Bian, Giant Topological Hall Effect in van der Waals Heterostructures of $\text{CrTe}_2/\text{Bi}_2\text{Te}_3$, *ACS Nano* **15**, 15710 (2021).
- [39] J. H. Jeon, H. R. Na, H. Kim, S. Lee, S. Song, J. Kim, S. Park, J. Kim, H. Noh, G. Kim, S.-K. Jeong, and S.-H. Chun, Emergent Topological Hall Effect from Exchange Coupling in Ferromagnetic Cr_2Te_3 /Noncoplanar Antiferromagnetic Cr_2Se_3 Bilayers, *ACS Nano* **16**, 8974 (2022).
- [40] Y. Ou, W. Yanez, R. Xiao, M. Stanley, S. Ghosh, B. Zheng, W. Jiang, Y.-S. Huang, T. Pillsbury, A. Richardella, C. Liu, T. Low, V. H. Crespi, K. A. Mkhoyan, and N. Samarth, $\text{ZrTe}_2/\text{CrTe}_2$: an epitaxial van der Waals platform for spintronics, *Nature Communications* **13**, 2972 (2022).
- [41] G. Kimbell, C. Kim, W. Wu, M. Cuoco, and J. W. A. Robinson, Challenges in identifying chiral spin textures via the topological Hall effect, *Communications Materials* **3**, 19 (2022).
- [42] D. Kan, T. Moriyama, K. Kobayashi, and Y. Shimakawa, Alternative to the topological interpretation of the transverse resistivity anomalies in SrRuO_3 , *Physical Review B* **98**, 180408 (2018).
- [43] M. Dreyer, J. Lee, H. Wang, and B. Barker, A low temperature scanning tunneling microscopy system for measuring Si at 4.2 K, *Review of Scientific Instruments* **81**, 053703 (2010).
- [44] S. J. Blundell, M. Gester, J. A. C. Bland, H. J. Lauter, V. V. Pasyuk, and A. V. Petrenko, Spin-orientation dependence in neutron reflection from a single magnetic film, *Physical Review B* **51**, 9395 (1995).
- [45] V. Lauter-Pasyuk, H. J. Lauter, B. Toperverg, O. Nikonov, E. Kravtsov, M. A. Milyaev, L. Romashev, and V. Ustinov, Magnetic off-specular neutron scattering from Fe/Cr multilayers, *Physica B: Condensed Matter* **283**, 194 (2000).
- [46] V. Lauter-Pasyuk, Neutron grazing incidence techniques for nano-science, *Collection SFN* **7**, s221 (2007).
- [47] V. Lauter, H. J. C. Lauter, A. Glavic, and B. P. Toperverg, Reflectivity, Off-Specular Scattering, and GISANS Neutrons, in *Reference Module in Materials Science and Materials Engineering*, edited by S. Hashmi (Oxford: Elsevier, 2016) pp. 1–27.
- [48] V. Lauter, H. Ambaye, R. Goyette, W.-T. Hal Lee, and A. Parizzi, Highlights from the magnetism reflectometer at the SNS, *Physica B: Condensed Matter* **404**, 2543 (2009).
- [49] C. Y. Jiang, X. Tong, D. R. Brown, A. Glavic, H. Ambaye, R. Goyette, M. Hoffmann, A. A. Parizzi, L. Robertson, and V. Lauter, New generation high performance in situ polarized ^3He system for time-of-flight beam at spallation sources, *Review of Scientific Instruments* **88**, 025111 (2017).
- [50] V. G. Syromyatnikov, V. A. Ulyanov, V. Lauter, V. M. Pusenkov, H. Ambaye, R. Goyette, M. Hoffmann, A. P. Bulkin, I. N. Kuznetsov, and E. N. Medvedev, A new type of wide-angle supermirror analyzer of neutron polarization, *Journal of Physics: Conference Series* **528**, 012021 (2014).
- [51] P. Giannozzi, S. Baroni, N. Bonini, M. Calandra, R. Car, C. Cavazzoni, D. Ceresoli, G. L. Chiarotti, M. Cococcioni, I. Dabo, A. Dal Corso, S. de Gironcoli, S. Fabris, G. Fratesi, R. Gebauer, *et al.*, QUANTUM ESPRESSO: a modular and open-source software project for quantum simulations of materials, *Journal of Physics: Condensed Matter* **21**, 395502 (2009).
- [52] J. P. Perdew, K. Burke, and M. Ernzerhof, Generalized Gradient Approximation Made Simple, *Physical Review Letters* **77**, 3865 (1996).
- [53] G. Pizzi, V. Vitale, R. Arita, S. Blgel, F. Freimuth, G. Granton, M. Gibertini, D. Gresch, C. Johnson, T. Koretsune, J. Ibaez-Azpiroz, H. Lee, J.-M. Lihm, D. Marchand, A. Marrazzo, *et al.*, Wannier90 as a community code: new features and applications, *Journal of Physics: Condensed Matter* **32**, 165902 (2020).

Supplementary Information for Strain-tunable Berry curvature in quasi-two-dimensional chromium telluride

Hang Chi,^{1,2} Yunbo Ou,¹ Tim B. Eldred,³ Wenpei Gao,³ Sohee Kwon,⁴ Joseph Murray,⁵ Michael Dreyer,⁵ Robert E. Butera,⁶ Alexandre C. Foucher,⁷ Haile Ambaye,⁸ Jong Keum,^{8,9} Alice T. Greenberg,² Yuhang Liu,⁴ Mahesh R. Neupane,^{2,4} George J. de Coster,² Owen A. Vail,² Patrick J. Taylor,² Patrick A. Folkes,² Charles Rong,² Gen Yin,¹⁰ Roger K. Lake,⁴ Frances M. Ross,⁷ Valeria Lauter,⁸ Don Heiman,^{1,11} and Jagadeesh S. Moodera^{1,12}

¹Francis Bitter Magnet Laboratory, Plasma Science and Fusion Center,
Massachusetts Institute of Technology, Cambridge, Massachusetts 02139, USA

²U.S. Army CCDC Army Research Laboratory, Adelphi, Maryland 20783, USA

³Department of Materials Science and Engineering,
North Carolina State University, Raleigh, North Carolina 27695, USA

⁴Department of Electrical and Computer Engineering,
University of California, Riverside, California 92521, USA

⁵Department of Physics, University of Maryland, College Park, Maryland 20742, USA

⁶Laboratory for Physical Sciences, College Park, Maryland 20740, USA

⁷Department of Materials Science and Engineering,
Massachusetts Institute of Technology, Cambridge, Massachusetts 02139, USA

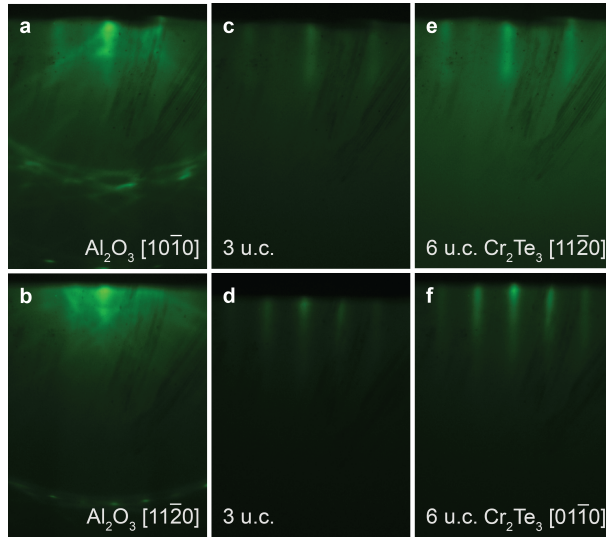
⁸Neutron Scattering Division, Neutron Sciences Directorate,
Oak Ridge National Laboratory, Oak Ridge, Tennessee 37831, USA

⁹Center for Nanophase Materials Sciences, Physical Science Directorate,
Oak Ridge National Laboratory, Oak Ridge, Tennessee 37831, USA

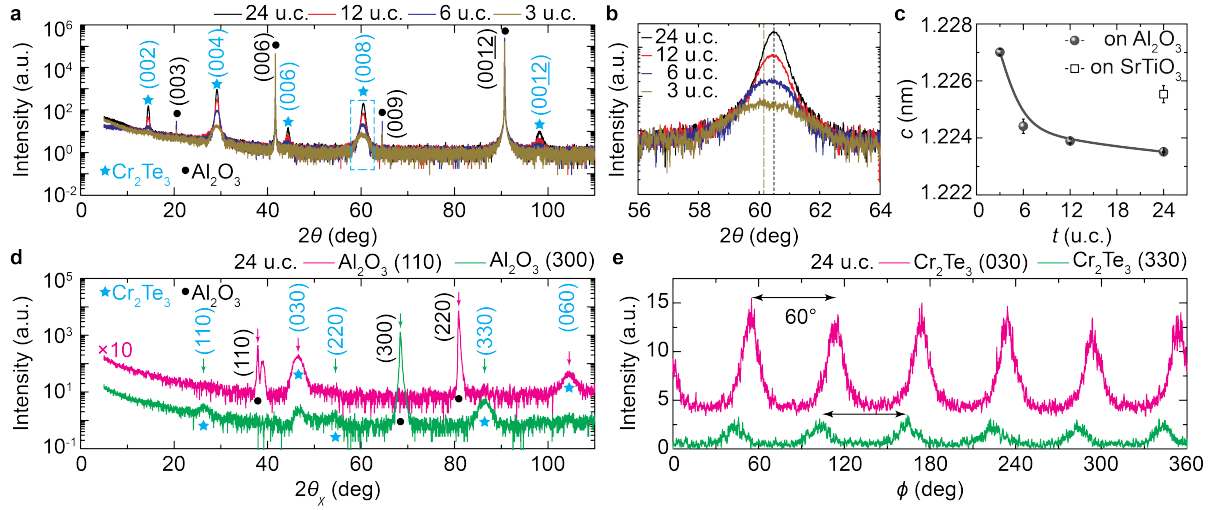
¹⁰Department of Physics, Georgetown University, Washington, District of Columbia 20057, USA

¹¹Department of Physics, Northeastern University, Boston, Massachusetts 02115, USA

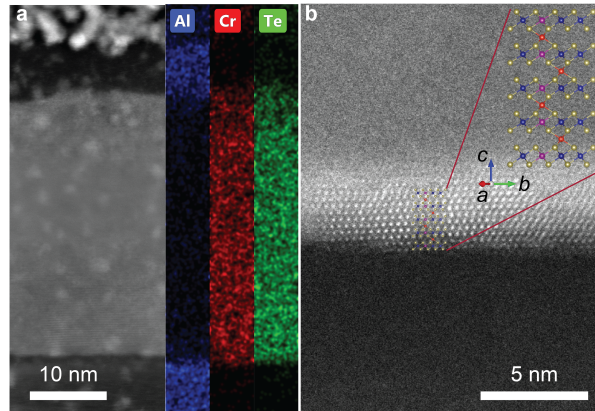
¹²Department of Physics, Massachusetts Institute of Technology, Cambridge, Massachusetts 02139, USA
(Dated: December 13, 2022)



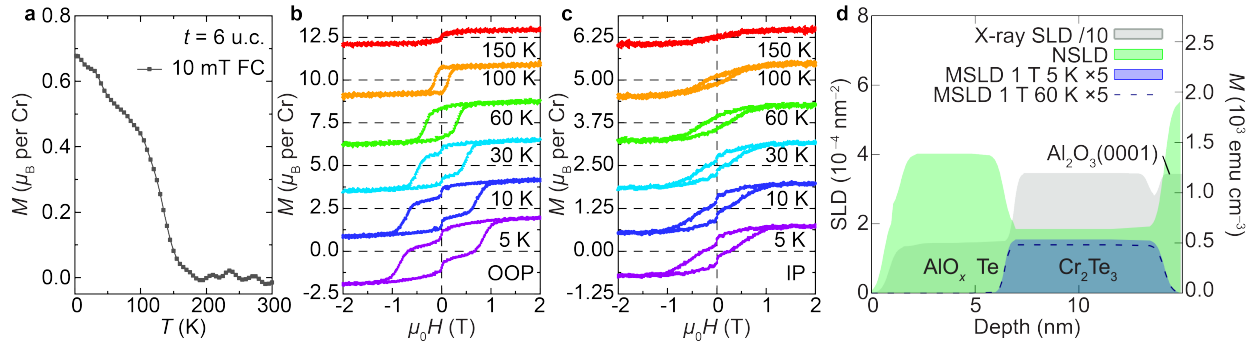
Supplementary Figure 1 | Reflection high-energy electron diffraction of Cr_2Te_3 . Typical *in situ* RHEED patterns from the surface of heat-treated $\text{Al}_2\text{O}_3(0001)$ substrates (a, b) and as-grown *c*-oriented Cr_2Te_3 (c-f) with thickness of 3 (c, d) and 6 (e, f) unit cell (u.c.). The incident electron beam is along the $[10\bar{1}0]$ (a, c, e) and $[11\bar{2}0]$ (b, d, f) crystalline orientations of Al_2O_3 , respectively. The clear Kikuchi lines in a and b attest to an atomically flat surface ready for the fabrication of high-quality epitaxial films. The corresponding RHEED patterns from the *c*-oriented Cr_2Te_3 (001) surface reveal sharp and streaky diffraction during the film deposition process, indicating the formation of a highly ordered and smooth surface as well as a 2D growth mode. Upon in-plane rotation, the same RHEED patterns reemerge every 60° , suggesting a six-fold crystalline symmetry within the basal plane of the as-grown films.



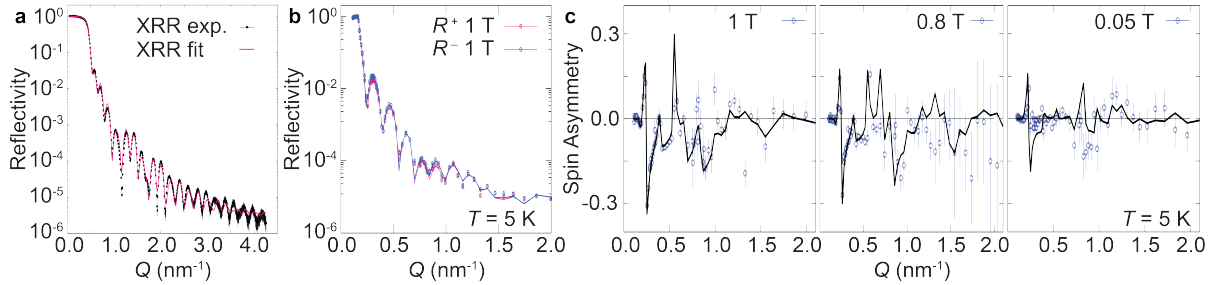
Supplementary Figure 2 | X-ray diffraction of Cr_2Te_3 . **a**, Out-of-plane $2\theta/\omega$ XRD patterns of c -oriented Cr_2Te_3 on $\text{Al}_2\text{O}_3(0001)$ with thickness $t = 3 - 24$ u.c.. **b**, Enlarged view of the (008) peaks showing gradual shift towards lower 2θ upon decreasing t . **c**, The t -dependence of the c lattice parameter indicating enhanced in-plane compressive strain at reduced t . **d**, In-plane $2\theta_x/\phi$ scans for $t = 24$ u.c. Cr_2Te_3 thin film, aligned with the Al_2O_3 (110) and (300) orientations. **e**, X-ray ϕ scans with $2\theta_x$ angle fixed at Cr_2Te_3 (030) and (330), respectively, corroborating the in-plane six-fold rotational symmetry. The lattice parameters are measured to be $a = b = 0.675 (\pm 0.002)$ nm and $c = 1.223 (\pm 0.004)$ nm, respectively, for $t = 24$ u.c..



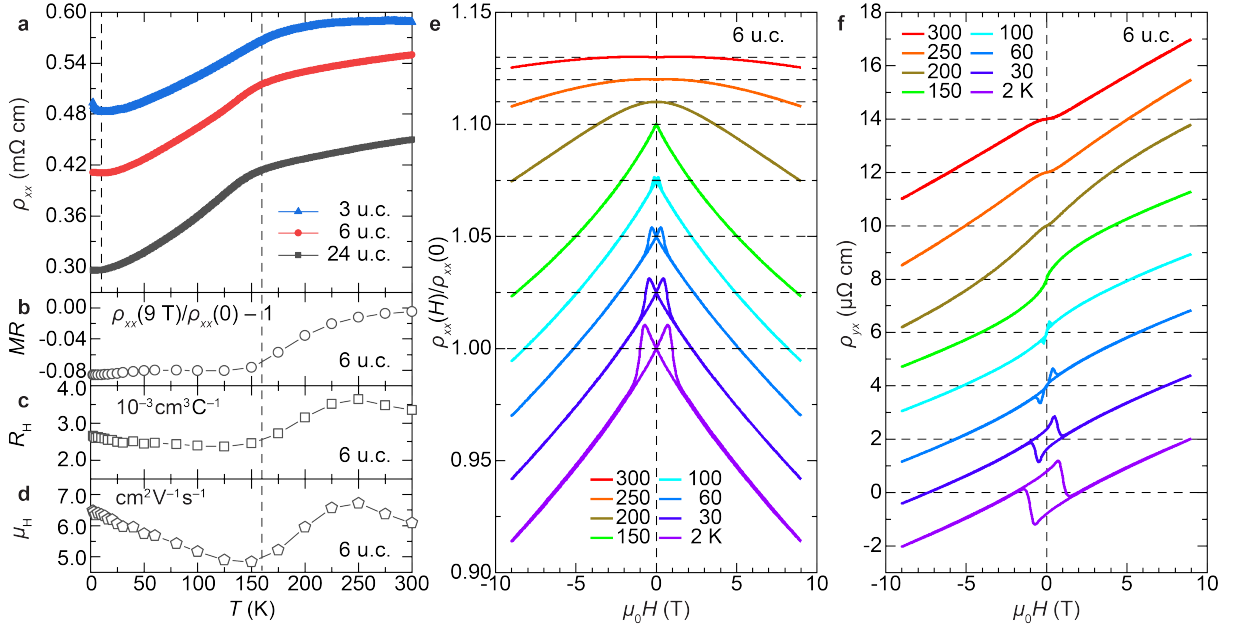
Supplementary Figure 3 | Scanning transmission electron microscopy of Cr_2Te_3 . **a**, Cross sectional STEM imaging of c -oriented Cr_2Te_3 on $\text{Al}_2\text{O}_3(0001)$ with thickness $t = 24$ u.c.. The energy dispersive X-ray spectroscopy (EDS) profile reveals a uniform elemental distribution. **b**, HAADF STEM image of a $t = 3$ u.c. sample illustrating the film quality.



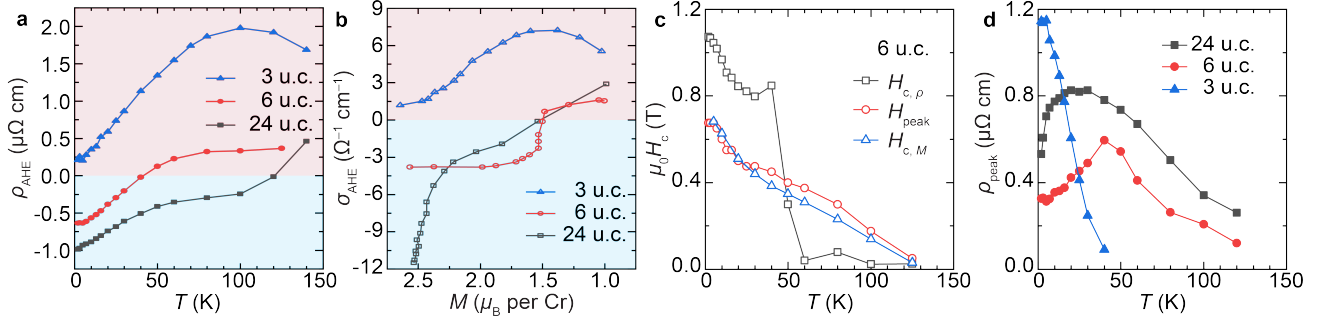
Supplementary Figure 4 | Magnetization of 6 u.c. Cr_2Te_3 . **a**, Temperature dependence of the magnetization M of 6 u.c. Cr_2Te_3 film under the field-cool (FC) condition with an out-of-plane (OOP) magnetic field $\mu_0 H = 10$ mT. **b-c**, Field dependence of M under OOP (**b**) and in-plane (IP, **c**) configurations, respectively, at selected T . Curves are vertically shifted for clarity. The preference of perpendicular magnetic anisotropy (PMA) is evident in the OOP $M(H)$ scans. **d**, Depth profiles of polarized neutron reflectometry (PNR) nuclear (NSLD), magnetic (MSLD, with IP $\mu_0 H = 1$ T at 5 K and 60 K, respectively) and X-ray scattering length densities (SLD) of 6 u.c. Cr_2Te_3 on $\text{Al}_2\text{O}_3(0001)$ substrate with Te/ AlO_x capping.



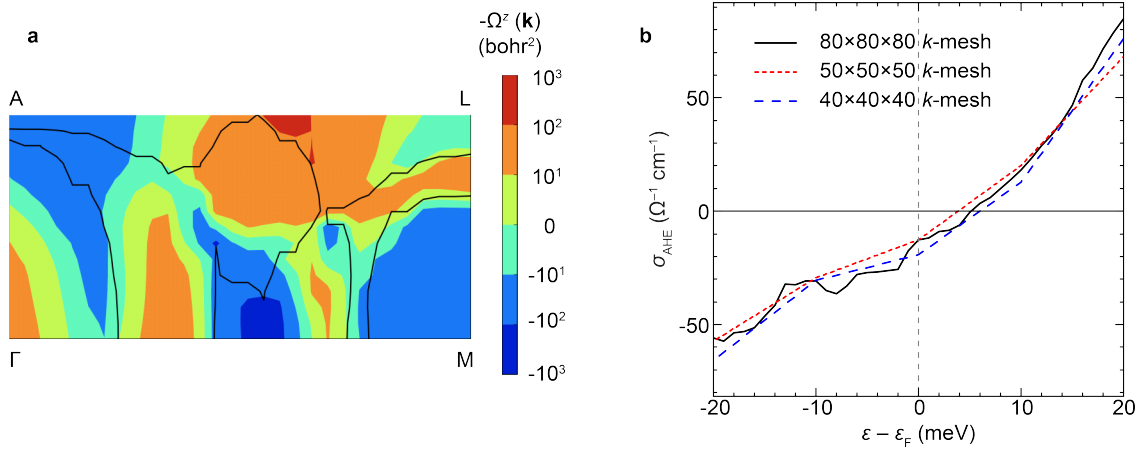
Supplementary Figure 5 | X-ray and polarized neutron reflectivity of 24 u.c. Cr_2Te_3 on $\text{Al}_2\text{O}_3(0001)$. **a**, Measured (points) and fitted (lines) X-ray reflectivity. **b**, Polarized neutron reflectivity at $T = 5$ K and $\mu_0 H = 1$ T. **c**, The PNR spin asymmetry ratio $SA = (R^+ - R^-)/(R^+ + R^-)$ for $\mu_0 H = 1$ T, 0.8 T and 0.05 T, respectively.



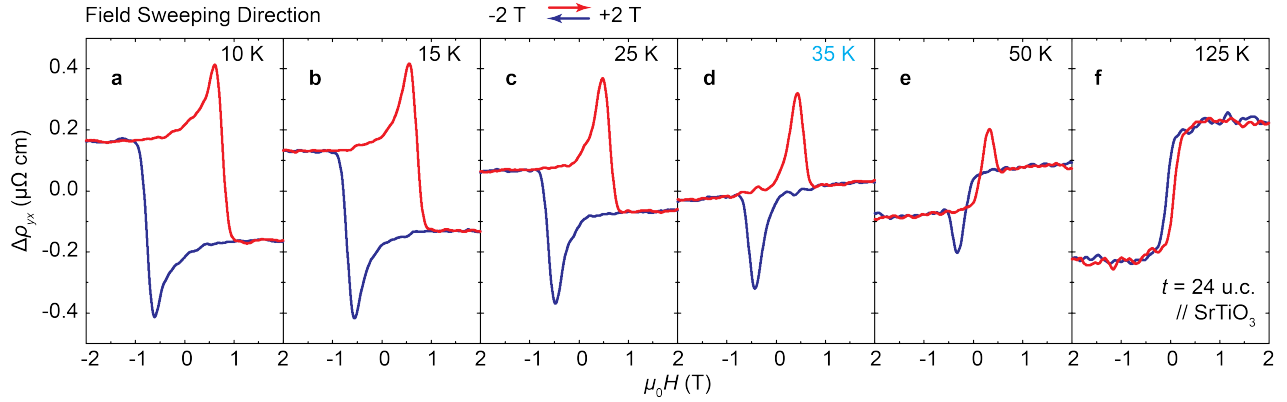
Supplementary Figure 6 | Transport properties of Cr_2Te_3 thin films. a, Temperature dependence of the longitudinal electrical resistivity $\rho_{xx}(T)$ of Cr_2Te_3 with $t = 3 - 24$ u.c.. b-d, The key transport parameters for $t = 6$ u.c., namely, the magnetoresistance [$MR \equiv \rho_{xx}(H)/\rho_{xx}(0) - 1$] at $\mu_0 H = 9$ T (b), the Hall coefficient R_H (c) and the Hall mobility μ_H (d) derived from the linear ordinary Hall effect at 8 – 9 T. e-f, Magnetic field dependence of $\rho_{xx}(H)$ (e) and the Hall resistivity $\rho_{yx}(H)$ (f) at selected temperatures for $t = 6$ u.c.. Curves in e-f are shifted vertically for clarity.



Supplementary Figure 7 | The characteristics of the unconventional Hall response of Cr_2Te_3 . a, Temperature dependence of ρ_{AHE} for $t = 24$ u.c. (black), 6 u.c. (red) and 3 u.c. (blue). b, The corresponding anomalous Hall conductivity σ_{AHE} as a function of the magnetization M . c, Temperature dependence of the field H_{peak} at which the hump-shaped peak occurs (red) for $t = 6$ u.c., along with the coercive fields $H_{c,\rho}$ (black) and $H_{c,M}$ (blue) determined from transport and magnetization measurements, respectively. d, Temperature dependence of the magnitude of the hump-shaped Hall feature ρ_{peak} .



Supplementary Figure 8 | Berry curvature and anomalous Hall conductivity in Cr_2Te_3 . **a**, Berry curvature contour plot of $-\Omega^z(\mathbf{k})$ with Fermi surface in the Γ -M-L-A k -plane. **b**, Convergence test of k -mesh for energy dependent σ_{AHE} near the Fermi level ϵ_F .



Supplementary Figure 9 | Hall response of 24 u.c. Cr_2Te_3 grown on $\text{SrTiO}_3(111)$. The Hall traces after removing the linear background at 10 K (a), 15 K (b), 25 K (c), 35 K (d), 50 K (e) and 125 K (f), respectively. Despite the choice of different substrate and hence distinct interface conditions, the temperature dependent anomalous Hall effect sign reversal and the unconventional hump-shaped Hall peaks are also present, attesting to the universality of the observed phenomena.